Supporting Information

Enwrapping $ZnIn_2S_4$ on vacancy-rich Nb_2O_5 nanoplate for enhanced photocatalytic hydrogen evolution

Yong-Qi Liu[a,§], Wen-Jing Yi[a,c,§], Chuan-Qi Li[b,c,], Xin Du[c], Zhong-Yi Liu[a,c], and Xin-Zheng Yue[c,]**

[a]School of Chemical Engineering, Zhengzhou University, Zhengzhou 450001, China.

[b]School of Chemistry and Chemical Engineering, Henan University of Technology, Zhengzhou 450001, China.

[c]College of Chemistry, Zhengzhou University, Zhengzhou 450001, China.

[§]Yong-Qi Liu and Wen-Jing Yi contributed equally to this work.

*Corresponding authors: lichuanqi@haut.edu.cn; yuexz@zzu.edu.cn

1. Experimental section

1.1. Chemicals and materials

Melamine ($C_3H_6N_6$, 99%), ammonium niobate (V) oxalate hydrate ($C_4H_4NNbO_9 \cdot nH_2O$, ≥99.9%), sodium sulfite (Na_2SO_3, 98%), indium chloride tetrahydrate ($InCl_3 \cdot 4H_2O$, 99.9%), zinc chloride ($ZnCl_2$, ≥98%), thioacetamide (TAA, ≥99%), and Nafion solution (5 wt%) were purchased from Aladdin. Ethanol (CH_3CH_2OH, ≥95.0%) and triethanolamine (TEOA, 98%) were bought from Shanghai Chemical Reagent Co., Ltd. Fluorine-doped tin oxide ($F:SnO_2$, FTO, <15 ohm sq^{-1}) glass was purchased from Zhuhai Kaivo Optoelectronic Technology Co., Ltd. N_2/H_2 (20 vol% of H_2) gas was purchased from Henan Yuanzheng Special Gas Co., Ltd. Deionized (DI) water (18.2 MΩ·cm) was prepared in the laboratory by instrument SZ-93A automatic pure water distiller (Shanghai Yarong biochemistry instrument factory).

1.2. Preparation of 2D Nb_2O_5 and v-NO nanoplates

In a typical experiment, 2.0 g of $C_4H_4NNbO_9 \cdot nH_2O$ and 2.0 g of melamine were added to a beaker containing 15 mL of ethanol. After overnight stirring, the mixture was dried in a vacuum oven at 60°C. The mixture was then calcined at 550°C for 4 h with a heating rate of 2°C min^{-1} in a muffle furnace. The powder of Nb_2O_5 was then obtained (Fig. S1). For achieving vacancy-rich Nb_2O_5 (donated as v-NO), the initially prepared Nb_2O_5 (0.2 g) was calcined in a tube furnace under an N_2/H_2 atmosphere at 600°C for 3 h with a heating rate of 2°C min^{-1}. Note that Nb_2O_5 and v-NO exhibit white and grey colors (Fig. S1), respectively.

1.3. Preparation of ZIS/v-NO and ZIS

$ZnIn_2S_4$/v-NO (ZIS/v-NO) was fabricated via a hydrothermal reaction. Specifically, when preparing ZIS/v-NO-30 (the mass fraction of v-NO is 30%), 0.100 g of v-NO, 0.540 g of $InCl_3 \cdot 4H_2O$, 0.272 g of $ZnCl_2$, and 0.300 g of thioacetamide were dissolved into 80 mL of HCl aqueous solution (pH = 2.5) with continuous stirring. Then, 20 mL of glycerol was added to the mixture and reacted at 80°C for 3 h. Following centrifugation and ethanol washing, the target product was collected. Additionally, the ZIS/v-NO-*x* (*x* = 10, 30, 50, and 90 wt%) were prepared by altering the quantities of v-NO to be 0.014, 0.043, 0.071, and 0.129 g, respectively, where *x* represents the mass fraction of v-NO. The ZIS/v-NO-30 sample in this study was labeled as ZIS/v-NO unless otherwise specified. For comparison, pristine $ZnIn_2S_4$ (ZIS) was also synthesized using a similar procedure without the addition of v-NO.

1.4. Characterization

The morphologies of photocatalysts were characterized using focused ion beam scanning electron microscopy (FIB-SEM, Zeiss auriga-bu, German) and transmission electron microscopy (TEM, FEI TalosF200S, Czech). The crystalline structure of samples was characterized by powder X-ray diffraction (XRD) with a Malvern Panalytical Empyrean (Netherlands) instrument using Cu Kα radiation (λ = 1.54056 Å) at 45 kV and 40 mA in the 2θ range of 5-90° at a scanning rate of 8° min^{-1}. Electron paramagnetic resonance (EPR) spectra were performed with an EPR spectrometer (EMX-9.5/12, German) at 298 K. X-ray photoelectron spectroscopy (XPS) measurements were carried out in a SPECS UHV system (German) equipped with a SPECS PHOIBOS 150 analyzer, a SPECS XR50 X-ray source and a SPECS 1D DLD detector using Al Kα excitation. C 1s of 284.8 eV was used to calibrate all XPS spectra. The UV-vis diffuse reflectance spectra (UV-vis DRS) were measured on a

UV-vis-NIR spectrophotometer (Shimadzu UV-3600) detecting absorption over the range of 200-800 nm. The steady-state photoluminescence (PL) emission spectra with an excitation wavelength of 320 nm were measured on a spectrofluorometer (FluoroMax-4, HORIBA, France). The specific surface areas and pore-size distribution were performed by the Brunauer-Enmet-Teller (BET) method on the basis of N_2 adsorption-desorption isotherms recorded on an instrument (JW-BK112, China) at a liquid nitrogen temperature (–196°C).

1.5. Photocatalytic H_2 generation

The photocatalytic H_2 generation experiments were tested with an all-glass automatic on-line trace gas analysis system (Labsolar-6A, Beijing Perfect Light Tec. Co., Ltd.) in a 300 mL quartz glass reaction cell containing 25 mg of photocatalyst, 90 mL of H_2O and 10 mL of TEOA, in which TEOA was used as a sacrificial reagent. To achieve uniform suspension, the mixture solution was sonicated for 10 min prior to reaction. Then, a 300 W Xe lamp (PLS-SXE300/300UV, Beijing PerfectLight Tec. Co., Ltd.) with cooling water (stabilize the temperature at 5°C) was served as light source to trigger the photocatalytic reaction and the suspension was continuously stirred to ensure uniform irradiation. H_2 gas generation was analyzed using an online gas chromatograph (GC-2014C, Shimadzu Co., Japan, with Ar as the carrier gas) equipped with an MS-5A column and a thermal conductivity detector (TCD). When visible light is utilized for photocatalytic H_2 generation experiments, a 420 nm cut-off filter was positioned in front of the lamp's lens, and the actual light power density was measured to be 654 W/m^2. For stability tests, nine cycles of 36 h were conducted, following the same procedure as described above for photocatalytic H_2 generation experiments. After every cycle was done, the system needs to be fully degassed until vacuumed. The apparent quantum efficiency (AQE) was measured at four

wavelengths (420 nm, 450 nm, 475 nm, and 500 nm) of monochromatic light, and calculated according to the following formula:

$$AQE = \frac{2N1}{N2} \times 100\%$$

where N1 and N2 represent the number of evolved H_2 molecules and the incident photons, respectively.

1.6. (Photo)electrochemical measurements

Typically, the (photo)electrochemical measurements were performed with a three-electrode system on an electrochemical workstation. The sample film on FTO, Pt wire and Ag/AgCl (saturated KCl) were served as the working electrode, counter electrode and reference electrode, respectively. To prepare of sample film, 10 mg of catalysts were thoroughly mixed with 375 μL of deionized water, 125 μL of ethanol and 50 μL of Nafion solution to get a slurry. Afterwards, 30 μL of slurry was evenly dropped onto the FTO substrate and calcined for 30 min at 250°C in an Ar atmosphere. For all the (photo)electrochemical measurements, 0.5 M Na_2SO_3 aqueous solution was used as the electrolyte. For photoelectrochemical (PEC) tests, the simulated solar light was supported by a 300 W Xe lamp equipped with an AM 1.5G optical filter. Electrochemical impedance spectroscopy (EIS) was conducted under light irradiation at potential of 0 V *vs*. Ag/AgCl over the frequency range from 100 kHz to 0.01 Hz with an amplitude of 5 mV. Open circuit potential (OCP) decay curves were performed after turning off the light irradiation, which were employed to analyze the charge decay behaviors. Current-time (*i-t*) curves were conducted with a light on/off cycle for every 40 s. Mott-Schottky (M-S) plots were tested under a frequency of 1000 Hz in dark condition.

1.7. SPV and TPV measurements

The lock-in-based surface photovoltage (SPV) spectrum was performed in a photovoltaic cell with a fluorine-doped tin oxide (FTO)-sample-FTO device under a 500 W Xe lamp (CHF-XM-500 W, Global Xenon Lamp Power) with a grating monochromator (Omni-5007, Zolix), a lock-in amplifier (SR830-D SP) and a light chopper (SR540). Transient photovoltage (TPV) measurements were conducted under a laser radiation pulse with the wavelength of 355 nm and pulse width of 5 ns from a third-harmonic Nd:YAG laser (Polaris II, New Wave128 Research, Inc.). The intensity of the pulse was read by a Joule meter (Starlite, Ophir, Inc.).

2. Supplemental Figures and Tables

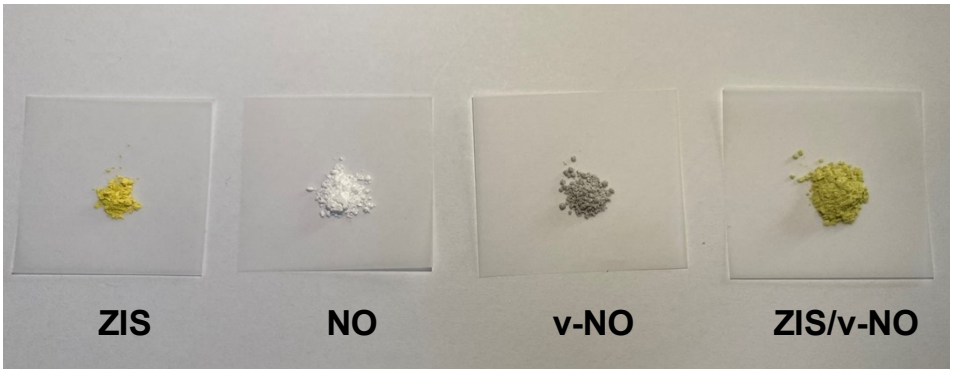

Fig. S1. Physical photographs of ZIS, NO, v-NO, and ZIS/v-NO catalysts.

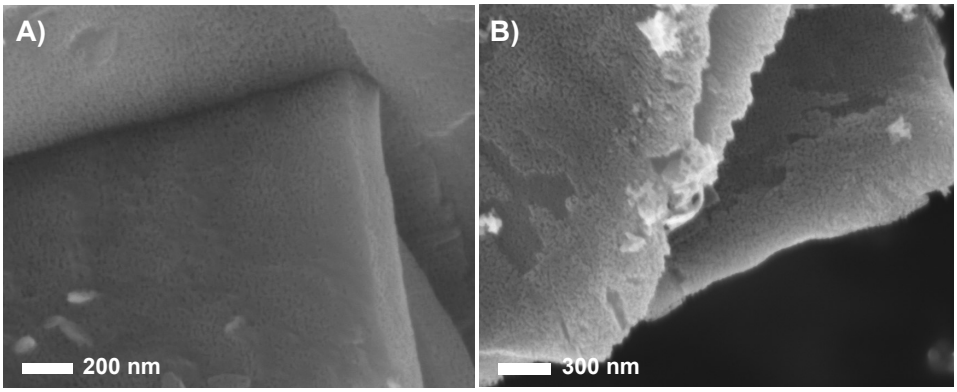

Fig. S2. FIB-SEM images of (A) NO and (B) v-NO.

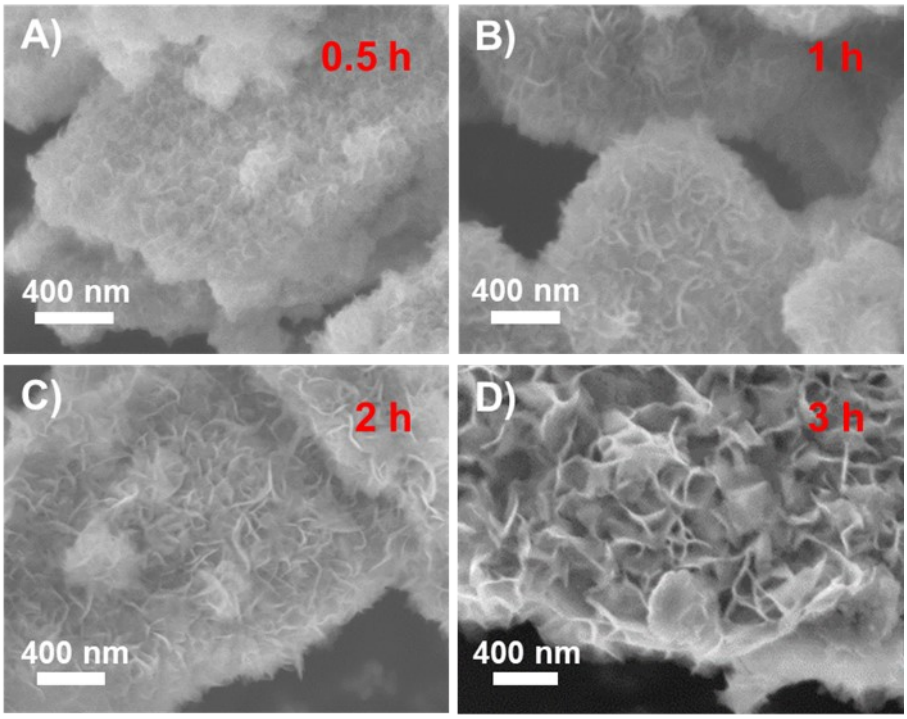

Fig. S3. FIB-SEM images of ZIS/v-NO composites synthesized at 80°C with different reaction time, (A) 0.5 h, (B) 1 h, (C) 2 h, and (D) 3 h.

As shown in Fig. S3, it can be clearly seen that ZIS nanosheets are uniformly dispersed and grown in situ on the surface of v-NO nanoplates to prepare ZIS/v-NO composites. During the hydrothermal progress, the morphology of prepared ZIS nanosheets becomes more distinct and their transverse size gradually increase with the increasing reaction time. Therefore, the reaction time influences the extent of ZIS growth and determines the thickness of ZIS/v-NO.

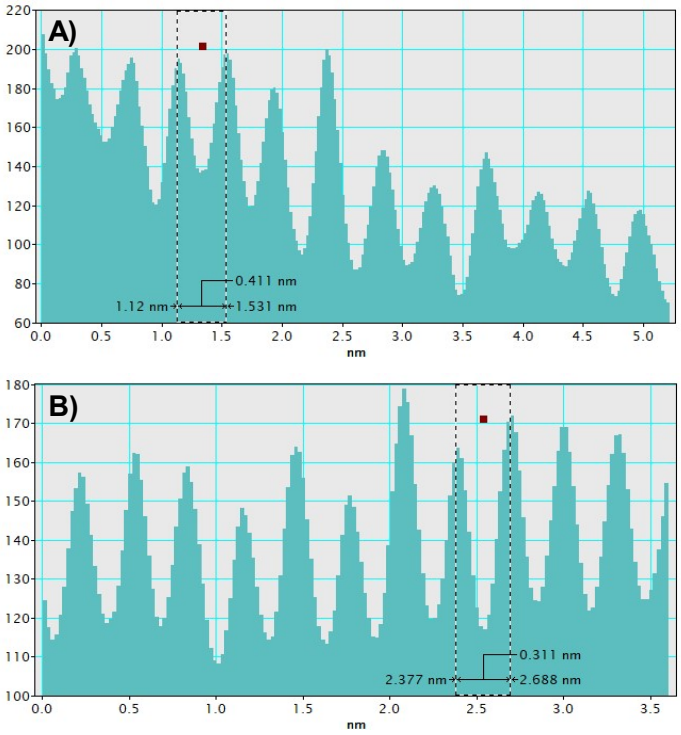

Fig. S4. HRTEM based line-intensity profiles of crystal fringes of (A) ZIS (006) plane and (B) NO (100) plane.

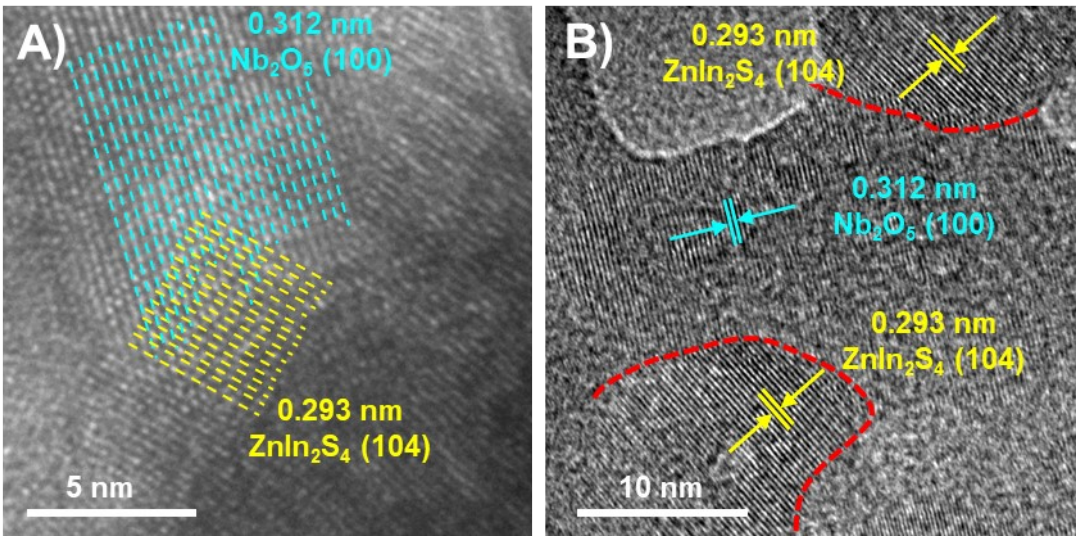

Fig. S5 HRTEM images of ZIS/v-NO.

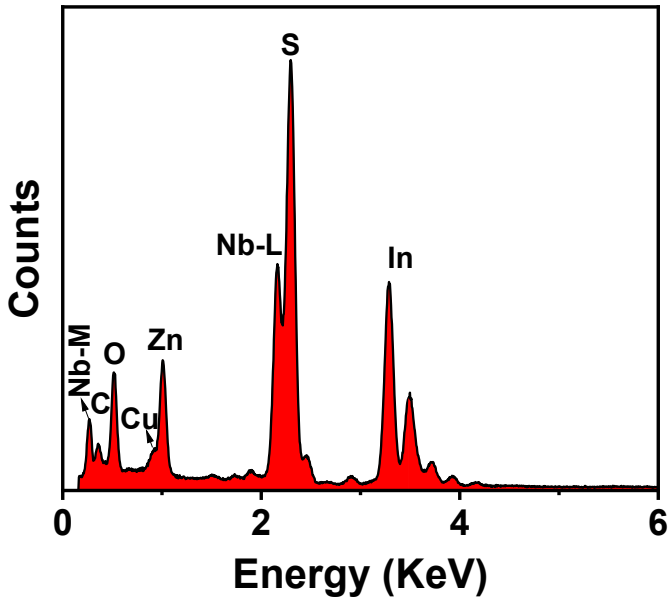

Fig. S6. EDX spectrum of ZIS/v-NO.

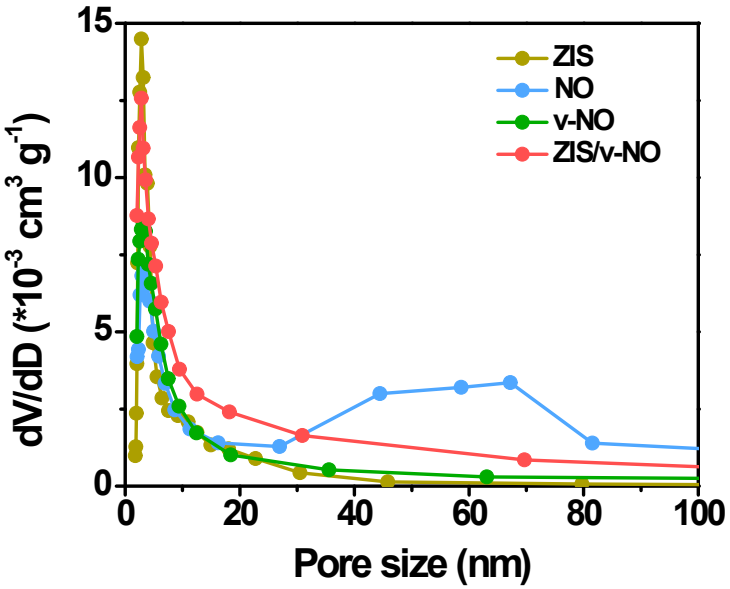

Fig. S7. Pore size distributions of ZIS, NO, v-NO, and ZIS/v-NO.

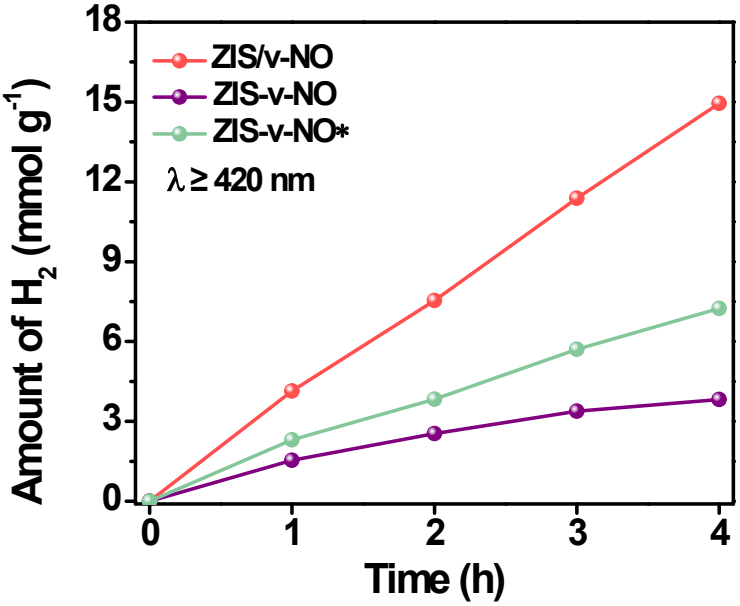

Fig. S8. Time-dependent photocatalytic H_2 evolution performance of ZIS/v-NO obtained from different preparation methods under visible light irradiation ($\lambda \geq 420$ nm).

To investigate the impact of the strong interaction formed in the ZIS/v-NO heterojunction on photocatalytic activity, we performed experiments to evaluate the performance of composites prepared using different methods. Here, a ZIS-v-NO composite was prepared by vigorously stirring a mixture of ZIS and v-NO in an ethanol solution, followed by drying. The sample denoted as ZIS-v-NO* was obtained by grinding the powers of ZIS and v-NO in a mortar. As displayed in Fig. S8, both ZIS-v-NO and ZIS-v-NO* exhibit significantly lower H_2-evolution activity and substantial decay in photocatalytic performance compared to that of ZIS/v-NO. These results demonstrate that the strong interfacial interaction within the ZIS/v-NO heterojunction can effectively enhance rapid separation and transfer of photogenerated charge carriers, thereby greatly improving photocatalytic efficiency.

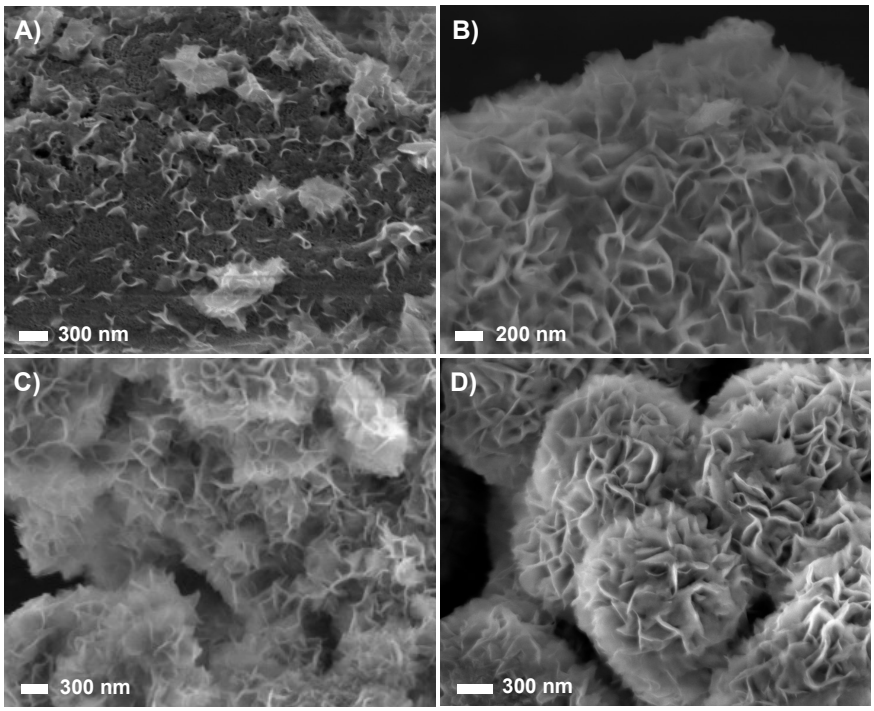

Fig. S9. FIB-SEM images of (A) ZIS/v-NO-90, (B) ZIS/v-NO-30, (C) ZIS/v-NO-10, and (D) ZIS.

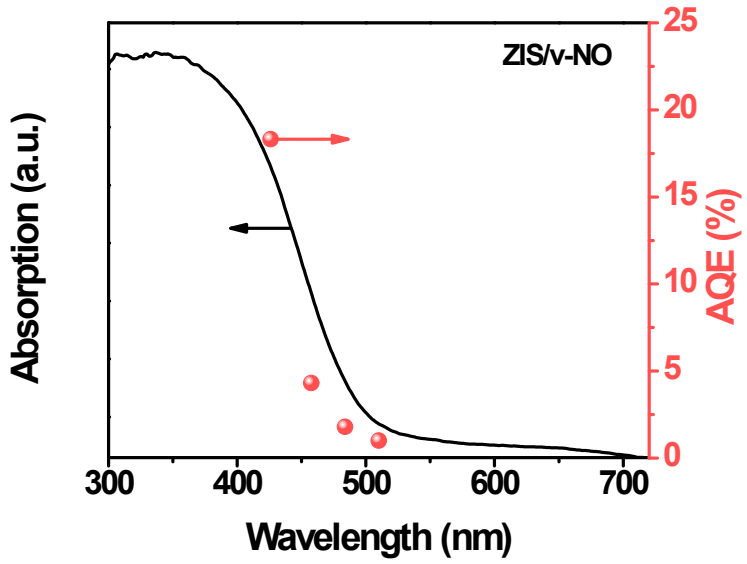

Fig. S10. UV-vis DRS (black line) and wavelength-dependent AQE (red symbols) of photocatalytic H_2 evolution over ZIS/v-NO.

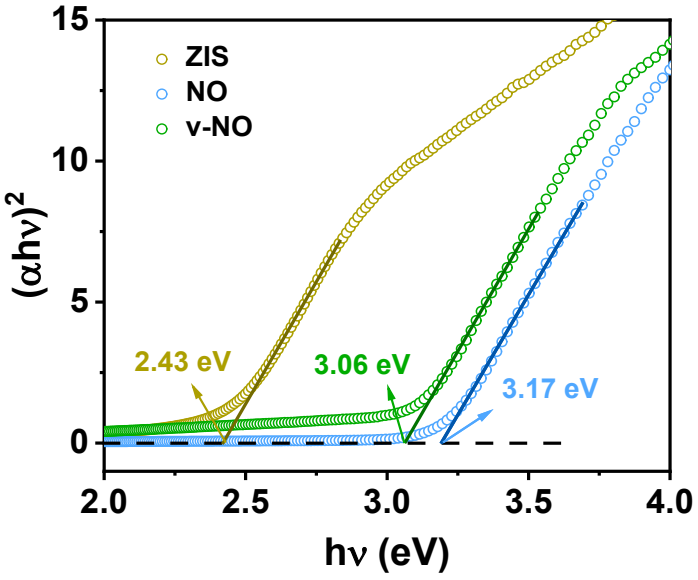

Fig. S11. The $(\alpha h\nu)^2$ versus $h\nu$ curves of ZIS, NO and v-NO obtained from UV-vis DRS.

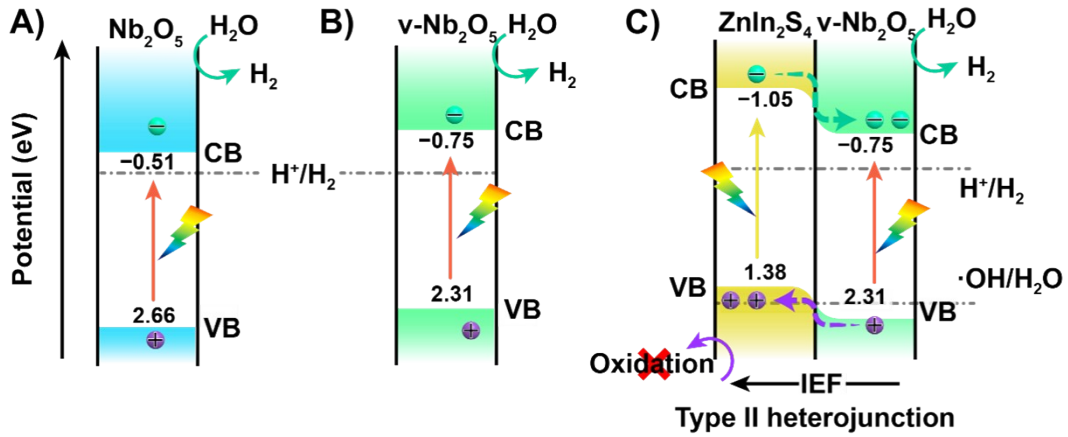

Fig. S12. The energy level diagrams of (A) NO, (B) v-NO, and (C) type II heterojunction of ZIS/v-NO.

Fig. S12 shows the energy level diagrams of NO, v-NO, and type II heterojunction of ZIS/v-NO. The negative E_{CB} of v-NO compared to NO indicates an enhanced reduction ability of photogenerated electrons in water reduction reaction for H_2 generation. If ZIS and v-NO forms the type II heterojunction (Fig. S12C), the CB-electrons of ZIS will flow towards v-NO, and correspondingly VB-holes of v-NO transfers towards ZIS. As a result, the reduction and oxidation reactions will occur at v-NO and ZIS, respectively.

3. Supplementary Tables

Table S1. Element contents of ZIS/v-NO obtained from EDX spectrum.

Element	Zn	In	S	Nb	O
Mass fraction (%)	10.63	36.35	22.30	26.46	4.26
Atomic fraction (%)	9.61	19.29	39.63	17.37	14.11

Table S2. Energy band structures of ZIS, NO and v-NO.

Sample	E_g (eV)	E_{CB} (V *vs.* NHE)	E_{VB} (V *vs.* NHE)
ZIS	2.43	–1.05	1.38
NO	3.17	–0.51	2.66
v-NO	3.06	–0.75	2.31

Table S3. Comparison of the photocatalytic H_2-evolution rate over ZIS and NO-based photocatalysts reported recently.

Photocatalyst	Reaction condition	H_2 evolution rate ($mmol\ g^{-1}\ h^{-1}$)	Cocatalyst	Ref.
$ZnIn_2S_4$/v-Nb_2O_5	**300 W Xe lamp (≥ 420 nm), 25 mg catalyst, 90 mL H_2O, 10 mL TEOA**	**3.70**	**-**	**This work**
8wt%Nb_2O_4/$ZnIn_2S_4$	300 W Xe lamp , 15 mg catalyst，40 mL H_2O, 7.5 mL TEOA	1.73	- ~2.3 wt% Pt	S1
TpBD COF/$ZnIn_2S_4$	300 W Xe lamp (≥ 420 nm), 25 mg catalyst，50 mL H_2O, 0.05 M Ascorbic acid	2.30	-	S2
C_3N_4/Nb_2O_5	300 W Xe lamp (> 400 nm), 50 mg catalyst，90 mL H_2O, 10 mL TEOA	1.71	1.5 wt% Pt	S3
g-C_3N_4@$ZnIn_2S_4$	300 W Xe lamp (≥ 420 nm), 50 mg catalyst，40 mL H_2O, 10 mL TEOA	2.78	-	S4

Co_3O_4@$ZnIn_2S_4$	300 W Xe lamp (AM 1.5G), 25 mg catalyst，45 mL H_2O, 5 mL TEOA	2.24	-	S5
Ag_2S-$ZnIn_2S_4$	300 W Xe lamp (> 420 nm), 25 mg catalyst，50 mL H_2O, 0.2 M Na_2S-Na_2SO_3	1.00	-	S6
$ZnIn_2S_4$@NH_2-MIL-125(Ti)	300 W Xe lamp (> 420 nm), 50 mg catalyst，100 mL H_2O, 0.35 M Na_2S + 0.25 M Na_2SO_3	2.20	-	S7
Ni_2P/$ZnIn_2S_4$	300 W Xe lamp (> 400 nm), 50 mg catalyst，100 mL H_2O, 10 mL Lactic acid	2.06	-	S8
$Zn_3In_2S_6$/F-C_3N_4	300 W Xe lamp (> 420 nm), 50 mg catalyst，100 mL H_2O, 0.35 M Na_2S + 0.25 M Na_2SO_3	0.51	2 wt% Pt	S9
COP-$ZnIn_2S_4$	300 W Xe lamp, 50 mg catalyst，50 mL H_2O, 0.35 M Na_2S + 0.25 M Na_2SO_3	0.95	-	S10
g-C_3N_4@$ZnIn_2S_4$	300 W Xe lamp with simulated sunlight, 10 mg catalyst，120 mL methanol solution, ($v(H_2O)$/v(methanol) = 90:30)	4.07	-	S11
$ZnIn_2S_4$/g-C_3N_4/Ti_3C_2	300 W Xe lamp (> 420 nm), 10 mg catalyst，8 mL TEOA, 72 mL H_2O	2.45	-	S12
$ZnIn_2S_4$/g-C_3N_4	300 W Xe lamp (> 420 nm), 50 mg catalyst，20 mL TEOA, 80 mL H_2O	3.21	-	S13
$Ti_3C_2T_X$/$ZnIn_2S_4$	300 W Xe lamp (> 420 nm), 20 mg catalyst，4 mL TEOA, 36 mL H_2O	3.47	3 wt% Pt	S14

References

S1 Y. Wang, X. Kong, M. Jiang, F. Zhang and X. Lei, A Z-scheme $ZnIn_2S_4/Nb_2O_5$ nanocomposite: Constructed and used as an efficient bifunctional photocatalyst for H_2 evolution and oxidation of 5-hydroxymethylfurfural, *Inorg. Chem. Front.*, 2020, **7**, 437-446.

S2 S. Bao, Q. Tan, S. Wang, J. Guo, K. Lv, S. A. C. Carabineiro and L. Wen, TpBD COF@$ZnIn_2S_4$ nanosheets: A novel S-scheme heterojunction with enhanced photoreactivity for hydrogen production, *Appl. Catal., B,* 2023, **330**, 122624.

S3 Q.-Z. Huang, J.-C. Wang, P.-P. Wang, H.C. Yao and Z.-J. Li, In-situ growth of mesoporous Nb_2O_5 microspheres on g-C_3N_4 nanosheets for enhanced photocatalytic H_2 evolution under visible light irradiation, *Int. J. Hydrogen energy,* 2017, **42**, 6683-6694.

S4 B. Lin, H. Li, H. An, W. Hao, J. Wei, Y. Dai and C. Ma, Preparation of 2D/2D g-C_3N_4 nanosheet@$ZnIn_2S_4$ nanoleaf heterojunctions with well-designed high-speed charge transfer nanochannels towards high-efficiency photocatalytic hydrogen evolution, *Appl. Catal., B,* 2018, **220**, 542-552.

S5 Y. Shi, L. Li, Z. Xu, F. Guo and W. Shi, Construction of full solar-spectrum available S-scheme heterojunction for boosted photothermal-assisted photocatalytic H_2 production, *Chem. Eng. J.,* 2023, **459**, 141549.

S6 J. Liu, G. Chen and J. Sun, Ag_2S-modified $ZnIn_2S_4$ nanosheets for photocatalytic H_2 generation, *ACS Appl. Nano Mater.,* 2020, **3**, 11017-11024.

S7 H. Liu, J. Zhang and D. Ao, Construction of heterostructured $ZnIn_2S_4$@NH_2-MIL-125(Ti) nanocomposites for visible-light-driven H_2 production, *Appl. Catal., B,* 2018, **221**, 433-442.

S8 X.-l. Li, X.-j. Wang, J.-y. Zhu, Y.-p. Li, J. Zhao and F.-t. Li, Fabrication of two-dimensional $Ni_2P/ZnIn_2S_4$ heterostructures for enhanced photocatalytic hydrogen evolution, *Chem. Eng. J.,* 2018, **353**, 15-24.

S9 Y. Wu, H. Wang, W. Tu, Y. Liu, S. Wu, Y. Z. Tan and J. W. Chew, Construction of hierarchical 2D-2D $Zn_3In_2S_6$/fluorinated polymeric carbon nitride nanosheets photocatalyst for boosting photocatalytic degradation and hydrogen production performance, *Appl. Catal., B,* 2018, **233**, 58-69.

S10 C. Cui, X. Zhao, X. Su, N. Xi, X. Wang, X. Yu, X. L. Zhang, H. Liu and Y. Sang, Porphyrin-based donor-acceptor covalent organic polymer/$ZnIn_2S_4$ Z-scheme heterostructure for efficient photocatalytic hydrogen evolution, *Adv. Funct. Mater.,* 2022, **32**, 2208962.

S11 Y. Xiao, B. Yao, M. Cao and Y. Wang, Super-photothermal effect-mediated fast reaction kinetic in S-scheme organic/inorganic heterojunction hollow spheres toward optimized photocatalytic performance, *Small*, 2023, **19**, 2207499.

S12 L. Wang, T. Yang, L, Peng, Q. Zhang, X. She, H. Tang and Q. Liu, Dual transfer channels of photo-carriers in 2D/2D/2D sandwich-like $ZnIn_2S_4$/g-C_3N_4/Ti_3C_2 MXene S-scheme/Schottky heterojunction for boosting photocatalytic H_2 evolution, *Chin. J. Catal.,* 2022, **43**, 2720-2731.

S13 Y. Qin, H. Li, J. Lu, Y. Feng, F. Meng, C. Ma, Y. Yan and M. Meng, Synergy between van der waals heterojunction and vacancy in $ZnIn_2S_4$/g-C_3N_4 2D/2D photocatalysts for enhanced photocatalytic hydrogen evolution, *Appl. Catal., B,* 2020, **277**, 119254.

S14 G. Zuo, Y. Wang, W. L. Teo, A. Xie, Y. Guo, Y. Dai, W. Zhuo, D. Jana, Q. Xian, W. Dong and Y. Zhao, Ultrathin $ZnIn_2S_4$ Nanosheets Anchored on $Ti_3C_2T_x$ MXene for Photocatalytic H_2 Evolution, *Angew. Chem. Int. Ed.,* 2020, **59**, 11287-11292.